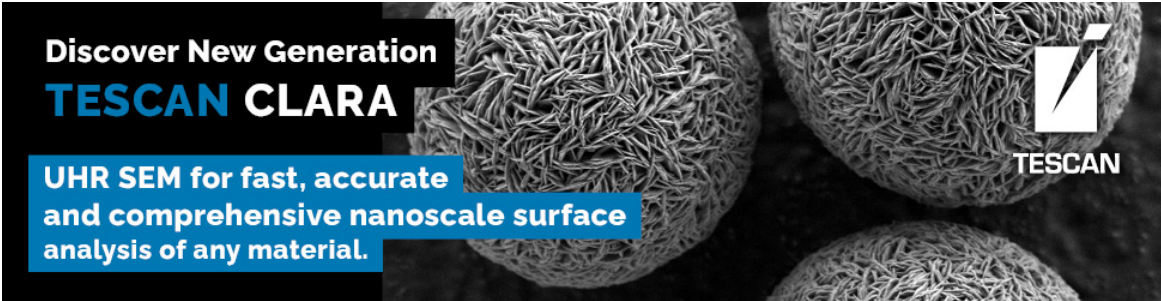# Electron-Beam-Induced Carbon Contamination in STEM-in-SEM: Quantification and Mitigation

Milena Hugenschmidt, Katharina Adrion, Aaron Marx, Erich Müller, Dagmar Gerthsen

Electron-Beam-Induced Carbon Contamination in STEM-in-SEM: Quantification and Mitigation

Milena Hugenschmidt[1,2,*], **Katharina Adrion**[1], **Aaron Marx**[1], **Erich Müller**[1] **and Dagmar Gerthsen**[1,2]

[1]*Laboratory for Electron Microscopy, Karlsruhe Institute of Technology (KIT), Karlsruhe, German*
[2]*3DMM2O – Cluster of Excellence (EXC-2082/1–390761711), Karlsruhe Institute of Technology (KIT), Karlsruhe, Germany*
Corresponding author: Milena Hugenschmidt, E-mail: milena.hugenschmidt@kit.edu

Abstract

Contamination is an undesired side effect in many electron microscopy studies that covers structures of interest and degrades resolution. Although contamination has been studied for decades, open questions remain regarding favorable imaging conditions for contamination minimization and the efficiency of contamination-mitigation strategies. This work focuses on electron-beam-induced carbon contamination in scanning transmission electron microscopy at electron energies of 30 keV and below. A reliable method to measure contamination thicknesses was developed in this work and enables the identification of imaging conditions that minimize contamination. Thin amorphous carbon films were used as test samples. The variation of important imaging parameters shows that the contamination thickness increases with the reduction of the electron energy to about 1 keV but decreases below 1 keV. Contamination increases with the beam current but saturates at high currents. Applying a given dose with a high dose rate reduces contamination. Among the tested contamination-mitigation methods, plasma cleaning and beam showering are most effective. Most experiments in this work were performed with focused scanning illumination. Experiments were also carried out with a stationary defocused beam for comparison with a theoretical contamination model with good agreement between measured and calculated contamination thickness.

Key words: carbon contamination, quantitative thickness measurement, sample cleaning, stem at low electron energies, STEM-in-SEM

Introduction

Electron-beam-induced carbon contamination is a detrimental side effect in almost all electron microscopy investigations. The growth of contamination is unwanted because it covers structures of interest, worsens the resolution, and may cause charging problems (Heide, 1963; Egerton, 2019). It also impedes analytical studies by energy-dispersive X-ray spectroscopy and electron energy loss spectroscopy that require high current densities. Contamination results from electron-beam-induced polymerization of carbon-rich organic molecules on the sample surface (mobile contaminants) that are present from sample preparation and storage or adsorption of molecules from the residual gas atmosphere in the microscope (Hillier, 1948; Heide, 1963; Egerton & Rossouw, 1976; Knox, 1976; Love et al., 1981; Reimer, 1998; Li & Joy, 2006). The contamination deposit is amorphous and carbonaceous but may contain other elements, like hydrogen, oxygen, or nitrogen (Hillier, 1948; Kumao et al., 1981; Reimer, 1998; Lau et al., 2010; Hettler et al., 2017). If a thin sample is irradiated by the electron beam, the deposit grows on both sides of the film (Hren, 1978).

A distinction must be made between contamination induced by three types of illumination: Illumination by a defocused stationary electron beam denoted as transmission electron microscopy (TEM)-like illumination in the following, illumination by a scanning focused beam denoted as scanning-(transmission)-electron-microscopy (S(T)EM)-like illumination, and illumination by a stationary focused electron beam (spot illumination). Different contamination morphologies typically result from different illumination strategies. For spot illumination, cones are formed (Conru & Laberge, 1975; Kanaya et al., 1990). Kanaya et al. and others described a transition from a cone to a circular frame-like morphology with increasing contamination thickness at the boundary of the illuminated region for an increasing beam diameter, depending on the relation between the spot radius and the diffusion coefficient (Hren, 1978; Kanaya et al., 1988). A large beam diameter frequently leads to circular, frame-like contamination patterns in TEM. For a focused scanning beam as in S(T)EM, the shape of the deposit typically follows the dimensions of the scanned area (Hirsch et al., 1994; Roediger et al., 2009). Its thickness is often more homogeneous than contamination from irradiating a region of the same size with a static beam, which was explained by the replenishment of hydrocarbons during the scan refresh time (Utke et al., 2008). However, amplified contamination growth at the border of the scanned region is also observed (Hirsch et al., 1994; Vladár et al., 2001, 2008; Vladár & Postek, 2005; Griffiths & Walther, 2010; Lau et al., 2010; Wanzenboeck et al., 2010).

Contamination research has been performed since the early studies of Stewart, Watson, and Ennos, and many other publications have shed light on different factors of carbon contamination (Stewart, 1934; Watson, 1947; Ennos, 1953). However, only a smaller fraction of the work is related to quantitative contamination studies. For example,

Hirsch et al. (1994) have systematically evaluated contamination growth in scanning electron microscopy (SEM) on bulk samples. They determined relative contamination thicknesses by recording backscattered electron (BSE)-SEM images that were normalized with the BSE intensity of clean sample regions. Roediger et al. (2009) investigated the absolute thickness of deposits produced by SEM irradiation on bulk Si by atomic force microscopy. Energy-filtered TEM was used for quantification of the contamination thickness by Mitchell who tested contamination growth on carbon films and other specimens at 200 keV in the STEM mode (Mitchell, 2015).

We focus in this work on contamination by S(T)EM-like illumination at electron energies of 30 keV and below, which are typically used in SEMs. In the following, we cite work that is concerned with the dependence of contamination on important imaging parameters. We also include results obtained for TEM-like irradiation. The contamination patterns obtained by TEM-like contamination are often different from S(T)EM-like illumination, but results on TEM-like irradiation provide valuable insights into contamination as well. Regarding the dependence of contamination on the *electron energy*, most studies reported a reduction of contamination thickness with increasing electron energy (Kumao et al., 1981; Hirsch et al., 1994; Roediger et al., 2009). This reduction can be understood by a lower yield of secondary electrons at higher energies (Lin & Joy, 2005; Smith, 2007) and the decrease in the probability for electron-induced dissociation of adsorbed molecules after a maximum in the 100 eV range (Alman et al., 2000; Fowlkes et al., 2005; Mitsuishi et al., 2005; van Dorp & Hagen, 2008). Others have stated no strong dependence of contamination on the primary electron energy, as long as the critical energies for ionization and dissociation of the contaminants are exceeded (Ennos, 1953; Hirsch, 1960; Ueda & Yoshimura, 2004), or an unclear behavior (Pinard, 2016). Even etching (removal of contamination) was reported for irradiation with <100 eV electrons (Mikmeková et al., 2016).

Contamination growth is regarded to be a diffusion-dependent process (Reimer & Wächter, 1978; Amman, 1996; Rykaczewski et al., 2007), although some authors disagree with this view (Kumao et al., 1981). Two contamination growth regimes can be distinguished depending on the *current density* (Christy, 1960; Rykaczewski et al., 2007; van Dorp & Hagen, 2008). One extreme is the reaction-limited regime, where the current density is so low that more contaminants reach the irradiated area than can be decomposed. The opposite extreme is the precursor-limited regime at higher beam currents, where all hydrocarbons are decomposed that reach the irradiated area. The transition of the growth regimes explains why contamination thicknesses increase up to a certain saturation level with increasing beam current (Ennos, 1953; Kumao et al., 1981). Others found decreasing or even vanishing contamination at very high current densities, which can be understood by an increasing sample temperature or electron-beam-induced sputtering that becomes dominant at high beam currents and electron energies (Egerton & Rossouw, 1976; Reimer & Wächter, 1978; Roediger et al., 2009; Mitchell, 2015).

Contamination frequently builds up approximately linear as a function of the *irradiation time* (Ennos, 1953; Egerton & Rossouw, 1976; Kumao et al., 1981; Hirsch et al., 1994; Rykaczewski et al., 2008; Horiuchi et al., 2009; Hettler et al., 2017). Directly after the start of irradiation, a higher growth rate is sometimes observed in the initial state (Conru & Laberge, 1975; Amman, 1996; Rykaczewski et al., 2007; Hettler et al., 2017). In other cases, a power-law dependence $\sim T^\alpha$ with $\alpha < 1$ over the full irradiation time T has been found (Ennos, 1953; Conru & Laberge, 1975; Knox, 1976; Tomita et al., 1979; Schiffmann, 1993; Mitchell, 2015).

Several techniques for *contamination mitigation* or sample cleaning are available today. Among those techniques are sample baking (McGilvery et al., 2012; Dyck et al., 2018; Goh et al., 2020), sample cooling (Egerton & Rossouw, 1976; Wall, 1980; Hirsch et al., 1994), plasma cleaning (Roberts et al., 1997; Isabell et al., 1999; Vladár et al., 2001; Horiuchi et al., 2009; Griffiths & Walther, 2010; McGilvery et al., 2012), beam showering (Amman, 1996; Hettler et al., 2017; Dyck et al., 2018), and UV cleaning (Hoyle et al., 2011; Soong et al., 2012; Hettler et al., 2017). Mitchell (2015) tested the efficiency of all methods mentioned above regarding their efficiency for 200 keV STEM on different samples, some of which were deliberately contaminated before the tests. He found that sample baking for several hours in an external vacuum chamber is moderately effective, making it a slow cleaning method, which also requires a clean pumping station. Cooling the sample to liquid-nitrogen temperature prevented contamination completely, yet the technique also is time-consuming and cooling stages are not frequently available in SEMs. He found plasma cleaning of the sample to be fast, but unable to remove all contaminants from carbon films, even when applied for more than an hour. Beam showering was observed to be fast and effective, although the effect only lasts for a limited time interval. Finally, UV cleaning was effective too, but time-consuming compared to plasma cleaning and beam showering. Other techniques to reduce contamination comprise, e.g., the use of cold traps (Hillier, 1948; Ennos, 1953; Heide, 1963), in-situ heating (Ennos, 1954; Hettler et al., 2017), washing the sample in solvents or a mixture of ethanol and activated carbon (Hirsch et al., 1994; Li et al., 2021), pre-bombardment with argon ions (Kanaya et al., 1988), a dry nitrogen leak, or nitrogen purge systems on the microscope (Postek, 1996), gas jets (Bance et al., 1978; Pinard, 2016), mechanical cleaning (of graphene) (Schweizer et al., 2020), and irradiation with <100 eV electrons (Mikmeková et al., 2016).

A theoretical description of contamination growth was developed by Müller (1969) and, based on Müller's work, Hirsch et al. (1994). They formulated a differential equation for electron-beam-induced contamination in an electron microscope. We note, however, that the model developed by Müller is only adequate for TEM-like illumination. It cannot be used for scanning illumination in SEM and STEM because the scanning electron beam leads to pixel-wise contamination that will overlap with increasing illumination time. Only scanning illumination with extremely short dwell times, usually not available in standard SEMs, can mimic stationary illumination of an area. The Müller and Hirsch models take adsorption and desorption of hydrocarbons into account, whereas other models only assume surface diffusion (Amman, 1996; Rykaczewski et al., 2007). Other theoretical approaches to electron-beam-induced (hydrocarbon) deposition, including Monte-Carlo (MC) methods, can be found (Fowlkes et al., 2005; Smith, 2007; Lobo et al., 2008; Pinard, 2016). Some of them were developed in the field of electron-beam-induced deposition, where a precursor gas is used to deliberately grow material on the specimen. These models are not used in this work due to the lack of analytical solutions.

This work focuses on contamination at low energies (30 keV and below) that are preferentially used in SEMs where, according to the literature overview above, contamination is typically more pronounced than at high electron energies. Numerous contamination studies were performed on bulk samples. However, systematic and quantitative contamination studies on STEM in scanning electron microscopes (STEM-in-SEM) are to our knowledge missing up to now. STEM measurements at low electron energies are meanwhile also performed in TEMs and will profit from our work as well (Sasaki et al., 2014; Sawada et al., 2015). We systematically investigate contamination as a function of relevant imaging parameters (electron energy, illumination time, electron-beam current (density), and total dose) to identify imaging conditions for minimum contamination and to further elucidate the mechanisms of contamination growth. The third goal focuses on the identification of cleaning strategies that minimize contamination growth.

Electron-transparent thin amorphous carbon films were used as test samples. The contamination thickness was quantitatively determined by taking STEM images with STEM detectors implemented in our STEM-in-SEM setup immediately after the contamination experiments without removing the sample from the instrument. For the quantification of contamination thicknesses, we have developed a method that is based on the comparison of high-angle annular dark-field (HAADF) STEM-in-SEM images with MC simulations. Our measurement setup was also applied to analyze the efficiency of different contamination-mitigation methods (beam showering, sample baking, and plasma cleaning). To address the reproducibility of contamination growth and monitor the status of the microscope, we suggest a test procedure that is applied before every measurement session. We also present some experiments with TEM-like illumination at low electron energies for comparison with calculated contamination thicknesses based on the analytical model by Müller (1969).

Materials and Methods

Theoretical Description of Contamination in Electron Microscopy

This section outlines an approach suggested by Müller to quantitatively describe contamination growth. Equation (1) considers the processes relevant for contamination growth. It is also helpful for the identification of the most relevant parameters and a deepened understanding of contamination. For this reason, we present the model here. However, an analytical solution of equation (1) is only available for homogeneous TEM-like illumination, while most of our experiments were carried out with scanning illumination in SEMs.

The description of contamination growth in electron microscopy is based on the assumption that a thin film of mobile molecules (contaminants) is adsorbed on the surface of most samples (Watson, 1947; Reimer, 1998). The molecules contributing to contamination growth were identified as hydrocarbons already in the 1940s (Watson, 1947; Hillier, 1948). Most important are –CH, –COOH, and –CNH2 compounds (Reimer, 1998). They stem from the ambient during sample storage and preparation steps, especially if solvents are used (Love et al., 1981; McGilvery et al., 2012; Soong et al., 2012; Mitchell, 2015). In addition, the residual gas atmosphere in the microscope can contribute to contamination when the vacuum is poor. Contaminants are only weakly bonded to the sample surface, presumably dominated by the van der Waals force, and can thus adsorb and desorb. Adsorption and desorption on the sample surface result in an equilibrium (Fig. 1a) (Hettler et al., 2017). The electron beam in an electron microscope disturbs the stationary state by decomposing the contaminants into fragments. They are then cross-linked (polymerized) on the sample surface, and a carbon-rich film starts to grow (Hillier, 1948; Reimer, 1998). Contamination growth leads to a gradient in the area density of contaminants, resulting in the diffusion of surrounding hydrocarbon molecules into the illuminated area (Fig. 1b). A steady state between the inflow of hydrocarbon molecules and their decomposition is reached after some time, and the contamination thickness increases with a constant growth rate (Fig. 1c). The steady state is characterized by a constant area density of contaminants in the irradiated and the surrounding area, although individual contaminants still diffuse. Hettler et al. (2017) found this state to be reached after around 30 s irradiation time (and an area electron dose of 200 C/cm^2). This time is not a general constant but depends, e.g., on the surface diffusion coefficient, the initial density of contaminants, and imaging parameters.

Contamination growth can be modeled by the approach developed by Müller (1969) and Hirsch et al. (1994). The differential equation below describes the change of the area density of molecules on the surface n as a function of time T. The equation takes into account the influence of adsorption, desorption, electron-beam illumination, and diffusion, driven by a concentration gradient Δn:

$$\frac{\partial n}{\partial T} = \underbrace{\frac{P}{\underbrace{\sqrt{2\pi m k_B \vartheta}}_{=v}}}_{\text{adsorption}} - \underbrace{\frac{n}{\tau_0}}_{\text{desorption}} - \underbrace{\frac{\sigma(E_0) \cdot j}{e} \cdot n}_{\text{electron beam}} + \underbrace{D \cdot \Delta n}_{\text{diffusion}}, \quad (1)$$

with partial pressure P of contaminants, molecular mass m of the contaminants, Boltzmann constant k_B, temperature ϑ, residence time τ_0 of molecules on the surface between adsorption and desorption, primary electron energy E_0, cross-section σ_c for decomposition and cross-linking the contaminants, and cross-section σ_d of electron-beam-driven desorption, in total $\sigma(E_0) = \sigma_c + \sigma_d$, electron-beam current density j, electron charge e, and diffusion constant D. We note that equation (1) is independent of the irradiation type. Müller solved it for n by assuming rotational symmetry, TEM-like irradiation, and a stationary case $\frac{\partial n}{\partial T} = 0$, which yields

$$n(r) = v \cdot \tau_0 \cdot \left(\frac{\kappa_0^2}{\kappa^2} + C \cdot I_0 \left(\frac{r}{\kappa_0} \right) \right), \quad (2)$$

with the radius of the irradiated area r, the modified Bessel function I_0, and the abbreviations

$$\kappa = \sqrt{\tau_0 \cdot D}, \quad \kappa_0 = \frac{\kappa}{\sqrt{1 + \frac{j\sigma}{eD} \cdot \kappa^2}} \ . \quad (3)$$

Notably, the definition of $n(r)$ differs slightly from the one in Müller's work, where κ^2 (in his notation ρ^2) was missing, possibly due to a printing error. The constant C is calculated from boundary conditions (Müller, 1969). Equation (2) describes the TEM-like case of circular and homogeneous irradiation.

The contamination thickness t_c as a function of irradiation time T and distance r from the center of irradiation can be
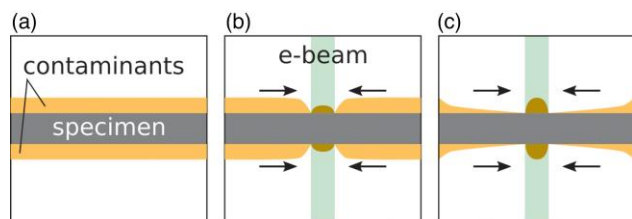
Fig. 1. Scheme of contamination growth and diffusion of contaminants into the area irradiated by the electron beam. (**a**) Initial state before irradiation, (**b**) conversion of contaminants into contamination, inflow of further contaminants into the irradiated area, and (**c**) steady state between the inflow of hydrocarbons and their decomposition (modified from Hettler et al., 2017).

calculated by equation (4), assuming a linear relation between T and t_c (Hirsch et al., 1994; Reimer, 1998)

$$t_c(r, T) = \frac{m_c}{\rho_c} \cdot \sigma_c \cdot \frac{j}{e} \cdot n(r) \cdot T. \quad (4)$$

m_c and ϱ_c are the molecular mass and material density of the deposited contamination. The calculated contamination thickness for TEM-like irradiation is compared with experimental results using TEM-like irradiation (cf. Section "Contamination for TEM-like Illumination and Comparison with Theory").

Contamination Experiments with S(T)EM- and TEM-Like Illumination

Amorphous carbon (aC) films with a thickness of 10 nm were used as test substrates for contamination growth. Commercial aC films were found to be pre-contaminated in an irreproducible way. Therefore, we prepared clean aC films ourselves. They did not show pre-contamination, while commercial aC films showed visible contamination in form of particles (see Supplementary Fig. 1). The thickness of the aC was measured by TEM from a cross-section TEM sample prepared by focused-ion-beam (FIB) milling. Details of the carbon-film and TEM sample preparation are given in the Supplementary Information.

Contamination patterns were grown and imaged in THERMO FISHER HELIOS G4 FX and FEI STRATA 400S dual-beam instruments (Thermo Fisher Scientific, Waltham, Massachusetts,

U.S.) at electron energies between 0.35 and 30 keV. As outlined in Section "Determination of the Contamination Thickness", these two instruments are additionally equipped with a STEM detector to acquire STEM images after the contamination test for the quantitative determination of the contamination thickness. No extra measures were taken to keep the microscopes clean. Specifically, repeated plasma cleaning of the microscope chamber could not be performed due to plasma-sensitive components in the chamber and the sample holder. Also, no cold traps were used because they are not routinely applied in SEMs. Both microscope chambers are pumped by turbomolecular pumps, the electron columns by ion getter pumps. Concerning gaseous precursors that are used for depositions in both instruments, it turned out that the chamber pressure decreases within one day into the standard range. According to our experience, contamination is not affected if experiments are performed after this time interval. We also consider leakage of the precursor unlikely while the FIB system is inactive because the material is not preheated.

The chamber pressure of the Helios microscope is typically between $1.7 \cdot 10^{-6}$ and $3.6 \cdot 10^{-6}$ mbar (see text in context with Fig. 4). The pressure values in the chamber of the Strata microscope are in a similar range. However, we note that the precision of pressure data obtained by the Penning gauges is limited, and the measurements were performed at the bottom of the microscope chamber a few centimeters away from the sample. We recognized that the microscope chamber conditions could not be kept constant and introduced reference measurements to monitor the changes (see Section "Reference Measurements to Monitor the State of the Chamber/Sample System").

Electron-beam patterns with scanning and homogeneous, stationary irradiation were defined to analyze contamination growth under S(T)EM- and TEM-like conditions. The S(T) EM-like test pattern is an electron-beam pattern of 3×3 squares with an area of $1\,\mu m^2$ each (Fig. 2a). The total dose was controlled by varying the irradiation time of the squares between 5 s and 10 min. Other parameter variations comprise the primary electron energy and electron-beam current (dose rate). We note that beam currents were measured by a Faraday cup because they may deviate from the nominal values.

The TEM-like test pattern consists of 3×3 circular patches with an area of $1\,\mu m^2$ each (Fig. 2b). For this purpose, the
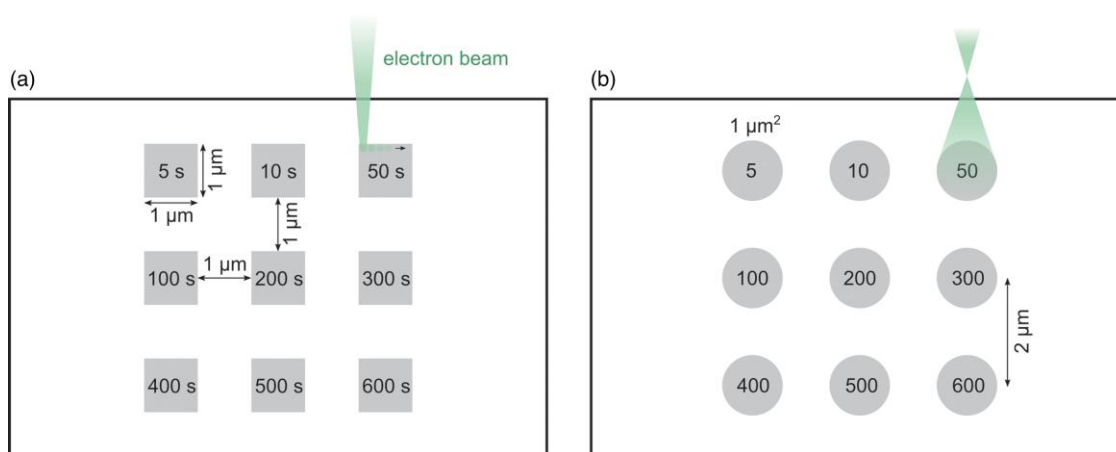

Fig. 2. Scheme of the electron-beam test patterns. The irradiated regions are shaded and cover an area of 1 μm^2. The numbers in the squares/circles give the irradiation time. (**a**) Scanning of squares with a focused electron beam. (**b**) Stationary circular irradiation with an over-focused electron beam.
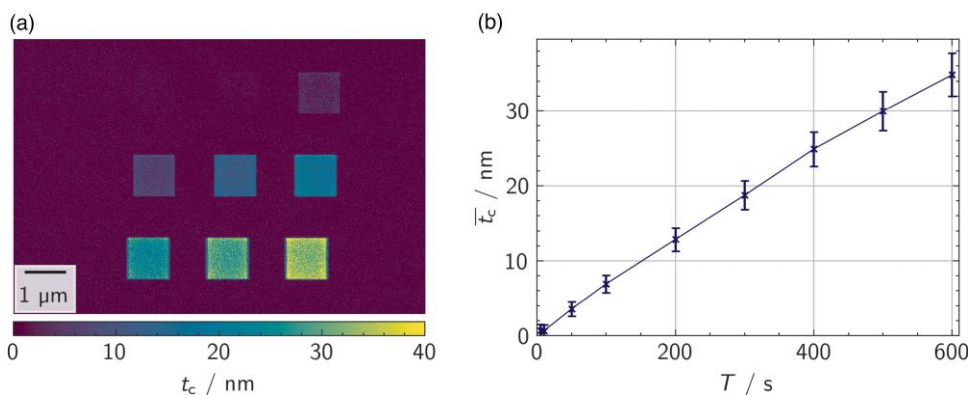
Fig. 3. S(T)EM-like contamination for 20 keV electron energy and 50 pA beam current (Helios). (**a**) Colorcoded contamination-thickness map for S(T)EM-like illumination according to the pattern in Figure 2a with increasing illumination time of the square patches from 5 to 600 s. The average thickness of the aC-support film is subtracted. (**b**) Average contamination thickness ($\overline{t_c}$) as a function of the irradiation time T.
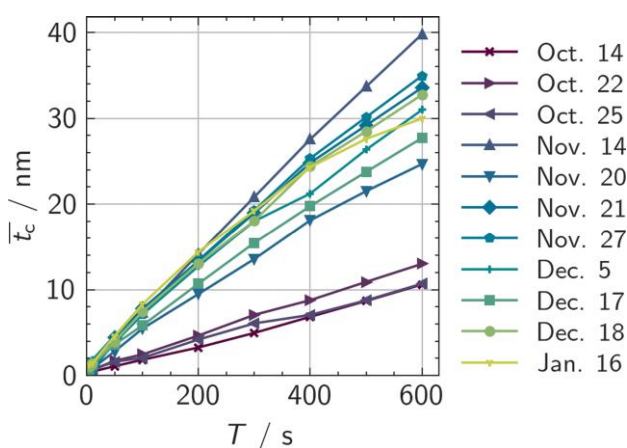

Fig. 4. Average contamination thickness ($\overline{t_c}$) as a function of the irradiation time T, measured on different days using the same imaging parameters and sample (aC film, Helios, 20 keV, 50 pA).

beam in the SEM was defocused to obtain circular patches and homogeneous irradiation, comparable to the irradiation in TEM. However, the beam has a smaller convergence angle. Again, irradiation times between 5 s and 10 min were chosen. This pattern fulfills the prerequisites of the model described in Section "Materials and Methods" [cf. Eqs (2) and (3)] for direct comparison of experimental and calculated data.

Experiments during this work have shown that the conditions regarding the microscope and the sample can change over weeks and months, e.g., after opening the microscope chamber or by contamination of the test sample during storage. Thus, reference measurements were established before any contamination experiment to test the state of the microscope and the aC film sample. For this purpose, S(T)EM-like test patterns were performed under the same conditions ($E_0 = 20$ keV, beam current in the Helios microscope 50 pA, beam current in the Strata microscope 40 pA) with exposure times indicated in Figure 2a. We selected 20 keV because it is a typical energy for STEM-in-SEM measurements, and the thickness determination based on STEM images is performed at this energy (Section "Determination of the Contamination Thickness"). Notably, the nominal beam currents of 50 and 40 pA are not identical with the real beam current, which is typically lower and was measured for each experiment using a

Faraday cup. Nevertheless, for the sake of clarity, we will refer to the nominal currents in the following, unless otherwise stated.

Determination of the Contamination Thickness

We used HAADF-STEM imaging to determine the thickness of the contamination deposits. The thickness determination requires the comparison of relative experimental and simulated HAADF-STEM intensities. MC simulations were used to calculate the relative HAADF-STEM intensity $I_{rel, sim}$ as a function of the aC thickness, as described in the Supplementary Information.

Contamination deposits on the electron-transparent aC film were imaged in the same microscope by HAADF-STEM. The contamination thickness was determined from the HAADF-STEM images acquired at 20 keV with the implemented STEM detector, which covers the scattering-range range between 68 mrad $< \theta \leq 272$ mrad (Helios microscope) and 168 mrad $< \theta \leq 617$ mrad (Strata microscope) at a working distance of 4.2 mm. Relative measured intensities I_{rel} are obtained from the intensity I in each pixel according to

$$I_{rel} = \frac{I - I_b}{c \cdot I_0 - I_b} \tag{5}$$

by subtracting the black-level intensity I_b obtained by averaging the intensity from the HAADF-STEM detector without exposure to electrons, and normalization with the intensity I_0 of the incident electron beam. The intensity of the incident electron beam was measured by directly scanning the HAADF segment of the STEM detector. The geometrical correction factor c takes into account inactive or blocked detector regions (Hugenschmidt et al., 2019), which is $c = 0.9205$ for the Helios and $c = 1$ for the Strata microscope.

The evaluation of relative intensities in HAADF-STEM images yields the thickness of the aC film and grown contamination by comparison with MC simulations, considering pure carbon with a density of 1.63 g/cm³ for the support film and the contamination (cf. Supplementary Information for the determination of the material density). The intensity of a HAADF-STEM image can then be converted into a contamination thickness map after subtraction of the aC-film thickness as illustrated in Figure 3a for S(T)EM-like illumination for the pattern shown in Figure 2a. We note that the thickness variation of our support film is negligibly small compared to the
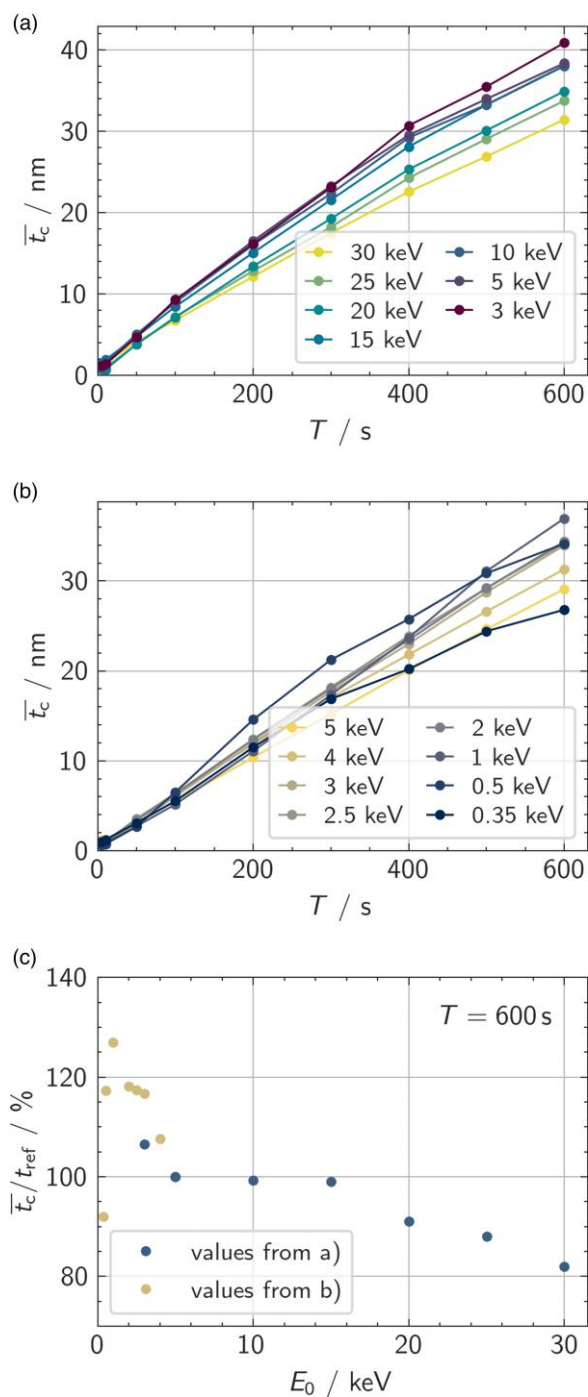
Fig. 5. Electron energy dependence of contamination on an aC film. (**a**) and (**b**) Average contamination thickness ($\overline{t_c}$) as a function of the irradiation time T for different E_0 using a beam current of 50 pA (Helios). The measurements in (**a,b**) were performed on two different days. (**c**) Average ($\overline{t_c}$)/t_{ref} as a function of E_0 for $T = 600$ s normalized with respect to the mean contamination thickness t_{ref} for $T = 600$ s at 5 keV.

beam finds the same density of contaminants at every position (Utke et al., 2008).

Contamination as a function of different imaging parameters and the effectiveness of contamination-mitigation strategies are compared in this work on the basis of average contamination thicknesses in each patch of the test patterns. The average contamination thickness $\overline{t_c}$ of each contamination patch was determined according to

$$\overline{t_c} = \frac{A_{pixel}}{A_{irr}} \cdot \sum_i N_i \cdot t_i, \qquad (6)$$

where N_i is the number of pixels with a contamination thickness t_i. The ratio A_{pixel}/A_{irr} of the area of one pixel and the irradiated area yields the inverse number of irradiated pixels. In general, the evaluated area of each contamination patch is chosen to be larger than $A_{irr} = 1 \, \mu m^2$, to take all contamination, including outside of the irradiated area, into account. Equation (6) implies that the total deposited contamination is normalized by the number of irradiated pixels. This ensures comparability between different measurements, even if the contamination thickness is inhomogeneous (e.g., for frame-like contamination) or if the grown contamination patch is distorted due to sample drift. This approach is also favorable compared to normalization by the number of evaluated pixels, since $\overline{t_c}$ would then depend on the size of the evaluated area and is not comparable with other measurements anymore.

Figure 3b shows that $\overline{t_c}$ increases with T and does not saturate in the investigated illumination time range. The error bars in Figure 3b were calculated by considering uncertainties of 0.8% on experimental gray values I, 0.9% on the measured intensity of the incident electron beam I_0, 1.2% on the black-level intensity I_b, and 6% on the slope of the simulated intensity curve due to possible uncertainties regarding the material composition or density. The uncertainty of the determined total thicknesses increases with increasing thickness and is found to be around ±6%. In the following thickness plots, the error bars will not be shown for clarity.

Results

Reference Measurements to Monitor the State of the Chamber/Sample System

The comparability of the microscope and sample conditions were always tested prior to contamination experiments by performing a reference measurement using the pattern in Figure 2a at 20 keV with nominal beam currents of 40/50 pA for the Strata and Helios microscopes, respectively. Figure 4 shows results of reference measurements on an aC film for the Helios microscope over three months. A significant variation of the contamination thickness as a function of illumination time is observed. The maximum contamination thickness was only 13 nm after 10 min of irradiation in October. The $\overline{t_c}$ curve increased strongly on the following date (Nov. 14), when a maximum contamination thickness of 40 nm was reached. After this, the maximum values varied between 25 and 35 nm. This shows that the state of the microscope and the sample change over time due to the storage of the sample and the use of the microscopes for other purposes in the meantime. We speculate that extended periods, in which the microscope is not under vacuum, may significantly influence contamination. However, a systematic increase in contamination and chamber pressure after venting the

average contamination thickness. The contamination thickness of all patches in Figure 3a is almost homogeneous compared to frame-like contamination patterns shown, e.g., in Figure 10, where contamination preferably occurs at the edges of the contamination patch. Homogeneous contamination can be understood by quickly diffusing hydrocarbon molecules replenishing also the central part of the irradiated region when the scanning beam is at another spot, such that the electron
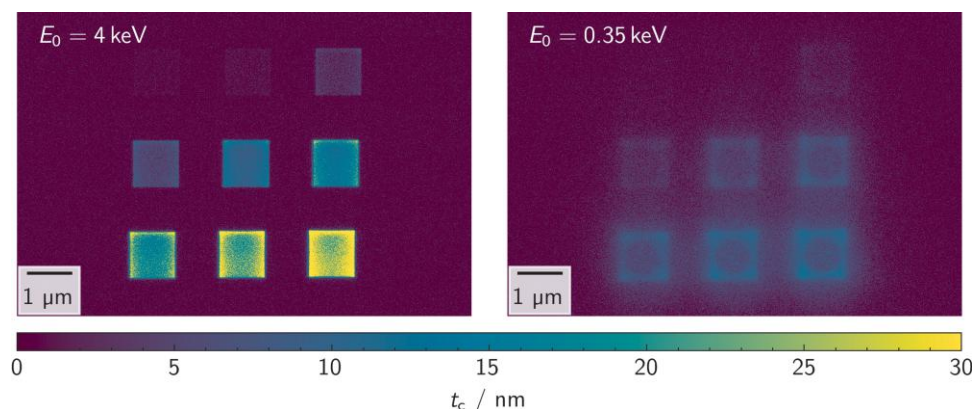
Fig. 6. Contamination-thickness maps grown on an aC film with $E_0 = 4$ keV and $E_0 = 0.35$ keV using the S(T)EM-like pattern in Figure 2a for a beam current of 50 pA (Helios).
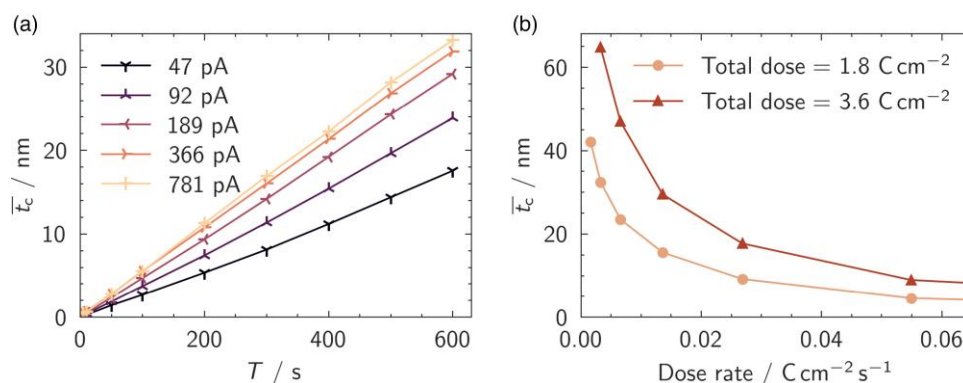

Fig. 7. Dependence of contamination growth on the beam current (dose rate) on an aC film. (**a**) Average contamination thickness ($\overline{t_c}$) as a function of the irradiation time T, grown with different beam currents (Helios, 20 keV). (**b**) Average contamination thickness ($\overline{t_c}$) of 1×1 μm^2 patches as a function of the beam current (Helios, 20 keV). The beam currents and irradiation time in (**b**) were varied (16 to 4,520 pA and 1,121 to 4 s) to keep the total dose constant at 1.8 C/cm^2 (circles) and 3.6 C/cm^2 (triangles). The doubled total dose (triangles) was achieved by doubling the irradiation time.

microscope chamber was not found. Moreover, the chamber pressure ranged between $1.7 \cdot 10^{-6}$ and $3.6 \cdot 10^{-6}$ mbar, but no correlation between chamber pressure and contamination could be observed. The sample may also contaminate during storage, as more contaminants adsorb on the sample surface.

The comparison of contamination tests in the two microscopes used in this work is shown in the Supplementary Information. Varying contamination thicknesses despite of using the same parameters (Fig. 4, Supplementary Fig. 4) demonstrate the necessity of reference measurements to keep track of the properties of the microscope/sample system. However, the variation of absolute contamination thicknesses does not limit the validity of the conclusions of this work because the general contamination behavior, e.g., the dependence on the tested parameters, was reproducible in many independent experiments conducted over a longer period. The results presented in the following include comparisons of different measurements. Directly compared data were mostly obtained on the same day. If results from different measurement sessions are compared, the comparability was checked with the reference measurements.

Contamination for S(T)EM-Like Irradiation

In the following subsection, we present results on the influence of relevant imaging parameters on contamination growth. Imaging strategies for minimum contamination are derived

from the quantitative measurements of the contamination thickness.

Influence of the Electron Energy

The primary electron energy E_0 is an essential parameter for contamination growth. Figure 5a shows the influence of E_0 between 3 and 30 keV. As expected, the contamination thickness increases with decreasing electron energy because the dissociation cross-section σ_d of different precursors is known to increase with decreasing E_0 until it reaches a maximum at low energies <1 keV (Alman et al., 2000; Fowlkes et al., 2005; van Dorp & Hagen, 2008). Therefore, it is interesting to investigate contamination at even lower energies between 0.35 and 5 keV, which is shown in Figure 5b. The absolute $\overline{t_c}$ values in Figures 5a and 5b cannot be directly compared because the measurements were performed on different days. However, a comparison is possible if the $\overline{t_c}$ data in both series are normalized with $\overline{t_c}$ at 5 keV and $T = 600$ s (denoted as t_{ref}). Figure 5c contains the normalized data at $T = 600$ s from the two-measurement series for higher and lower energies, where reduced contamination at electron energies below 1 keV is visible.

Analyzing the contamination-thickness maps at 4 keV (Fig. 6a) and 0.35 keV (Fig. 6b), we observe a change of the contamination morphology at low electron energies. At 4 keV, the contamination is confined to the irradiated squares and looks homogeneous with only slightly thicker and
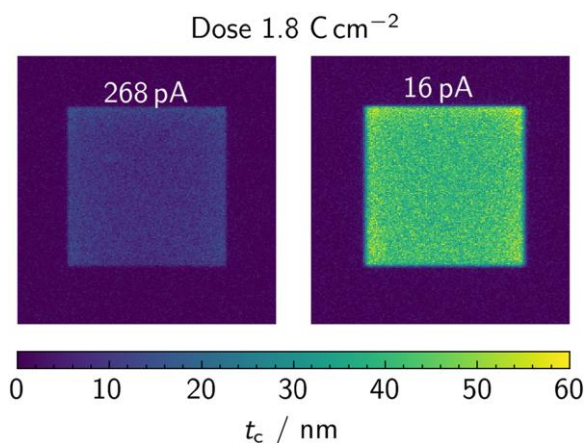
Fig. 8. Contamination-thickness maps for patches illuminated at 20 keV with 268 pA within 68 s (left) and 16 pA within 1,121 s (right), yielding the same total dose (Helios).
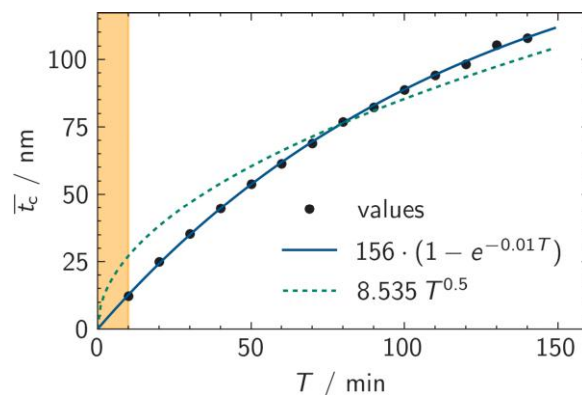

Fig. 9. Average contamination thickness ($\overline{t_c}$) as a function of the irradiation time T for a long irradiation time up to 140 min (aC film, Strata, 20 keV, 40 pA). The orange region marks the time interval up to 10 min, which is the maximum irradiation time in the other experiments.

well-defined borders. At 0.35 keV, the contamination is mainly concentrated at the border of the illuminated patches, where in-diffusing molecules are already polymerized before they reach the center of the patches. Contamination is clearly observed in the regions between the irradiated squares. We attribute the spread of contamination to charging because more electrons are absorbed at very low electron energies. If the conductivity of the support film is too low, these charges are not transported away. The charging causes inhomogeneous electric fields in the film and its vicinity, which interact with the electron beam and may lead to spreading contamination. Another reason for the changed contamination pattern may be the enhanced emission rate of secondary electrons, having a maximum at 0.4 keV in carbon (Lin & Joy, 2005), and an enhanced emission rate of backscattered electrons tested by the CASINO MC software (Demers et al., 2011). It is unlikely that the spread results from the strong increase of the probe diameter at low energies, as shown by the following consideration. At an electron energy of 350 eV, diffraction is the dominant effect that determines the beam diameter. With the used convergence angle of 7 mrad and an electron wavelength of 65 pm, the beam diameter at the first minimum of the Airy function is only 24 nm. Therefore, even with the contribution of side maxima of the Airy intensity distribution, the large extent of contamination between the patches with a distance of 1 μm cannot be explained. Notably, a cleaning effect of preparation residuals on graphene by low-energy electrons has been observed at 0.5 keV (Materna Mikmeková et al., 2020). Although we did not observe a cleaning effect, the reduction of contamination in our studies indicates a change in the contamination behavior at very low electron energies. However, electron energy reduction below 1 keV is not a good strategy to mitigate contamination of aC because charging disturbs the imaging process - apart from resolution loss due to the increase in the beam diameter. In addition, the electron energy of 0.35 keV results in a comparable contamination thickness as for 20 keV. Hence, E_0 should be maximized to reduce contamination growth.

Influence of the Electron-Beam Current and Total Electron Dose

Figure 7a shows $\overline{t_c}$ as a function of illumination time for different measured beam currents between $I = 47$ pA and $I =$

781 pA and an electron energy of 20 keV. $\overline{t_c}$ does not depend linearly on the beam current. This is also illustrated in Figure 8 where contamination-thickness maps for patches are shown, which were illuminated with the same total dose of 1.8 C/cm² using different beam currents and illumination times. This areal dose is calculated on the basis of the complete irradiated area, not the beam diameter. It is the product of beam current and irradiation time divided by the irradiated area. This means that we neglect the time dependency of scanning and treat the irradiation as a constant irradiation of the scanned area. The patch illuminated with the larger beam current within a shorter time shows significantly less contamination than the other patch. Further contamination patches for two different total doses were evaluated and are presented in Figure 7b, showing that contamination thickness decreases with increasing dose rate and, as expected, with the reduction of the total dose.

All three figures (Figs. 7a, 7b, 8) demonstrate that contamination thickness is not a pure effect of the total dose but depends strongly on the time that is needed to apply this dose (the dose rate). Applying a high current in a short time yields less contamination than a low current applied in a long irradiation time. This result indicates that the contamination growth is not only determined by the number of electrons, but also by the number of contaminants that reach the irradiated area. Accordingly, two extreme growth regimes can be distinguished: The electron-limited and the precursor-limited regime (Christy, 1960; van Dorp & Hagen, 2008). In the electron-limited regime, more contaminants (precursors) reach the irradiated area than can be immobilized and converted to contamination. The growth rate thus only depends on the current density. In the precursor-limited regime, there is a depletion of contaminants in the irradiated area, because the beam converts all contaminants that reach the area. Under these conditions, a higher current does not increase the contamination growth, as it only depends on the diffusion of new contaminants into the irradiated area. The third regime is a mixture of the two extremes (Rykaczewski et al., 2007; Utke et al., 2008). The current and dose tests indicate that we are in the transition between the electron-limited and the precursor-limited regime because higher currents increase the contamination thickness up to 189 pA (electron-limited). The growth saturates if the current is further increased
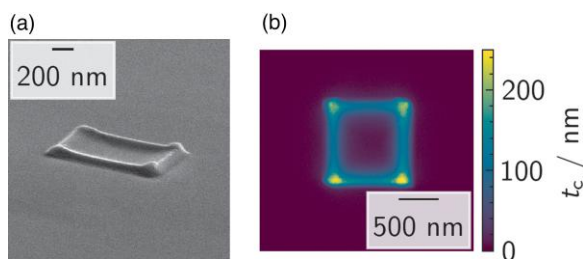
Fig. 10. (**a**) 3 keV SE-SEM image of a contamination patch grown over 140 min (20 keV, Strata, 40 pA). The viewing direction is tilted 70° away from the top view. (**b**) Corresponding contamination-thickness map.

(precursor-limited). A temperature rise of the specimen at higher currents may also contribute to the saturation (Kumao et al., 1981). This can be explained by the temperature dependency of the interaction cross-section $\sigma(E_0)$, which determines, similarly to the current j, the interaction of the electron beam with the contaminants. Sputtering of the sample can also contribute to the reduction of contamination growth. However, we attribute the saturation of contamination thicknesses to the limited supply of contaminants, as we have not observed sample thinning.

A method to reduce contamination while keeping the total dose (and, e.g., the counts in energy-dispersive X-ray spectra) constant is the application of a high dose rate in a short time.

Saturation of Contamination

Up to now, contamination growth was investigated only for irradiation times T up to 600 s. The growth proceeds linear in a good approximation in agreement with the model outlined in Section "Materials and Methods". In contrast to this model, Mitchell (2015) proposed a parabolic rate relationship between irradiation time T and contamination thickness

$$t_c = K \, T^{0.5} + c \tag{7}$$

where K is a rate constant and c a starting constant that describes an incubation period in the beginning, during which the contamination rate may be lower.

Figure 9 shows the $\overline{t_c}$ as a function of T for a square patch, which was irradiated for up to 140 min at 20 keV with 40 pA. The illumination was interrupted regularly to acquire HAADF-STEM images for thickness determination. The measured data are fitted using equation (7). We assume $c = 0$ due to the long overall illumination time and the first thickness measurement after 10 min. The best possible parabolic fit (dashed green line, fit function in the legend of Fig. 9) disagrees with the experimental data. Instead, the contamination thickness increases almost linearly up to 50 min and slows down for longer illumination times. This behavior is well described by the fit of a restricted growth function with an upper limit at $t_{max} = 156$ nm. Figure 9 validates the assumption of $t_c \propto T$, at least for irradiation times below 50 min.

Morphology of Contamination

Figure 10a shows a secondary electron (SE)-SEM image of the topography of a contamination patch, which was grown over 140 min. The contamination-thickness map of the same patch is shown in Figure 10b. Both images reveal frame-like contamination growth with stronger contamination at the edges and corners and less contamination in the center, which results

from the depletion of contaminants in the center of the irradiated area. At the edges and corners, contaminants from the non-irradiated surroundings can diffuse towards the irradiated patch, leading thus to enhanced contamination. However, this behavior is less pronounced for shorter irradiation times (10 min, Supplementary Fig. 5), where a sufficient concentration of contaminants is still available in the vicinity of the contamination patch. For long illumination times, the vicinity of the illuminated patch is increasingly depleted from contaminants reducing the number of contaminants that can reach the center of the patch.

Contamination growth on the top and bottom surfaces of the thin aC support is expected because most beam electrons propagate through the thin aC film and the growing contamination. A cross-section TEM study was performed for the patch with the contamination-thickness map in Figure 11a to investigate the shape of a contamination patch in more detail. A cross-section TEM specimen was prepared along the orange line by the FIB-based procedure described in the Supporting Information. The bright-field (BF-)STEM image in Figure 11b shows the whole patch in a cross-section perspective. The contamination and aC film in the center appear bright. The dark layers above and below are Pt layers deposited by sputter deposition to stabilize the aC film and the deposited contamination. Pt-rich protection layers that appear less dark were deposited by electron-beam and FIB-induced deposition during TEM sample preparation (Fig. 11c). The cross-section images show that contamination grows almost symmetrical on both sides of the aC film. The gradual thickness increase at the border of the contamination patch is also seen in Figures 11b and 11c and stems from sample drift in horizontal direction during contamination growth.

Contamination for TEM-Like Illumination and Comparison with Theory

TEM-like test patterns according to Figure 2b are used for comparison with calculated contamination thicknesses according to the model presented in Section "Materials and Methods". An experimental contamination-thickness map obtained for $E_0 = 20$ keV, $I = 32$ pA, and T between 5 and 600 s is shown in Figure 12a. The patches show pronounced frame-like contamination, in contrast to S(T)EM-like contamination patches using similar parameters (Fig. 3a), where an almost homogeneous contamination thickness is observed. This finding can be well understood because continuous illumination by a defocused electron beam leads to pinning of contaminants already at the border of the electron beam in contrast to scanning illumination where hydrocarbons at each scan position can be replenished during the scan refresh time (Utke et al., 2008).

The contamination thickness of the circle illuminated for 600 s (bottom right circle in Fig. 12a) is azimuthally averaged and plotted as a function of the radius in Figure 12b. The measured contamination thickness was fitted using equation (4) for the set of parameters given in Table 1. The contamination is supposed to be carbon with a density of 1.63 g/cm³. For the comparison with the model, the contaminants were assumed to be C_3H_8 with its atomic mass given in Table 1 because this molecule was identified, among others, in the mass spectrum obtained from the residual gas atmosphere in the microscope chamber (Supplementary Fig. 6). We are aware that the molecules found in the mass spectrum can be
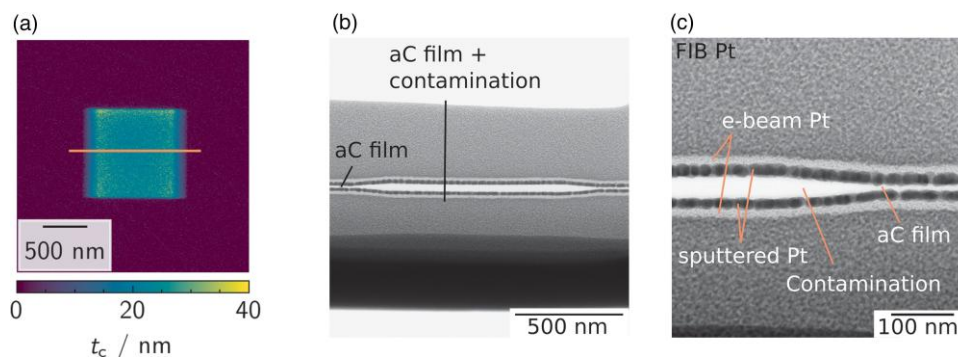
Fig. 11. (**a**) Contamination-thickness map of a patch that was grown over 10 min (20 keV, Helios, 50 pA) and used for cross-section TEM analysis. The line marking indicates the location of the cross-section sample that was prepared from the patch. (**b,c**) overview and high-magnification 200 keV BF-STEM images of the cross-section TEM sample of the contamination patch in (**a**) prepared along the line.
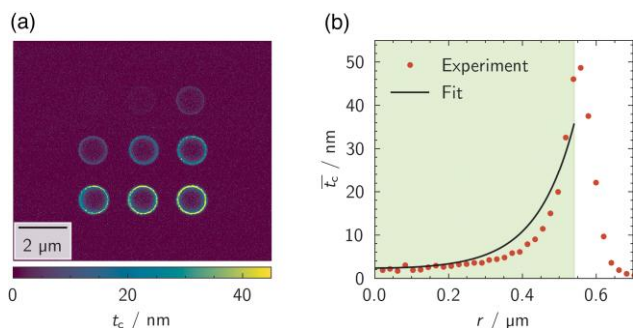

Fig. 12. Measured and calculated contamination thicknesses for TEM-like illumination with a stationary and defocused electron beam according to the pattern in Figure 2b. (**a**) Experimental contamination-thickness map with increasing illumination time between 5 s (top right) and 600 s (bottom left) (20 keV, Strata, 32 pA), and (**b**) azimuthally averaged contamination thickness of the circular contamination patch grown for 600 s (dots) and calculated thickness (line) using the parameters in Table 1. The irradiated area is marked by shading.
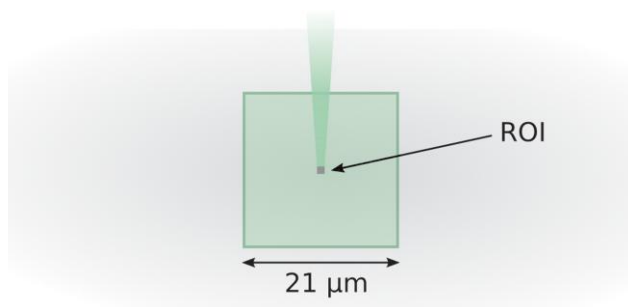

Fig. 13. Concept of beam showering. A region of ~$21 \times 21 \ \mu m^2$ (indicated by the large square) around the ROI is scanned for 10 min. Immediately afterward, a field of $1 \times 1 \ \mu m^2$ (ROI) is scanned, and the contamination thickness is evaluated every 120 s.

fragments of larger hydrocarbons and are not necessarily the original contaminant species (Wanzenboeck et al., 2010). The diffusion constant D is taken from the measurement presented in Section "Strategies for Contamination Mitigation". Electron-beam-driven desorption of contaminants is neglected by setting $\sigma_d = 0 \ Å^2$ (van Dorp & Hagen, 2008). The dissociation cross-section σ_c was calculated for C_3H_8, according to

Alman et al. (2000), considering the contribution of direct dissociation and dissociative ionization as well as the two surfaces of the film. $E = 20$ eV was assumed as average energy of SE, which have the highest dissociation probability due to their low energy, and the SE yield of 0.08 for carbon at 20 keV was taken from Lin and Joy, which leads to $\sigma_c = 0.76 \ Å^2$ (Lin & Joy, 2005).

The unknown parameter partial pressure P of the contaminant molecules is set to $P = 1 \cdot 10^{-7}$ mbar, a realistic value considering that the partial pressure of contaminants is a fraction of the total pressure of typically $5 \cdot 10^{-6}$ mbar in the microscope chamber. The parameters listed in Table 1 leave the residence time τ_0 between adsorption and desorption of contaminants on the surface as the only fit parameter. The residence time is determined by a least-squares fit of the experimental data yielding $\tau_0 = 84$ s. This value is consistent with the lower limit of 10 s for the residence time of hydrocarbons found by Hirsch (1977). It is long enough to explain why surface diffusion plays a significant role in contamination. The experimental results show a steeper increase towards the border of the irradiated area than the calculated curve, which indicates that the assumed D could be too large. Assuming a smaller D than the measured surface diffusion coefficient yields a better-fitting curve (not shown in Fig. 12b) and a larger value for τ_0. Although the calculated thicknesses and the fit result depend on the reliability of the other parameters, the comparison with theory is helpful to confine the order of magnitude of otherwise unknown parameters.

Strategies for Contamination Mitigation

In the following section, we use our method for the quantitative determination of contamination thickness to analyze and compare the efficiency of different contamination-mitigation strategies (beam showering, (external) sample heating (baking), and plasma cleaning). The techniques are also discussed with respect to their ease of use. By analyzing the contamination growth after beam showering, we could obtain an estimate for the surface diffusion constant of contaminant molecules in our experiments.

Instead of the 3×3 pattern used for the measurements above, a single square of $1 \times 1 \ \mu m^2$ was irradiated to evaluate sample cleaning methods. The total illumination time of the patch was 20 or 36 min. The temporal development of contamination growth was studied by regular interruptions every 120 s to image the contamination patch. Thin aC films were used for all cleaning tests.

Table 1. Parameters Used to Calculate the Contamination Thickness in Figure 12b.

Parameter	Value
j	35 A/m^2
m	$7.32 \cdot 10^{-26}$ kg (C$_3$H$_8$)
m_c	$1.99 \cdot 10^{-26}$ kg (C)
ϑ	293 K
ϱ	1.63 g/cm^3
D	$1.5 \cdot 10^{-14}$ m^2/s
σ_d	0 Å^2
σ_c	0.76 Å^2
P	$1 \cdot 10^{-7}$ mbar
τ_0	**84 s**

The fitted parameter τ_0 is highlighted in bold.

Beam Showering and Estimation of the Surface Diffusion Constant of Contaminants

Beam showering is a strategy to reduce contamination growth by preventing contaminants from reaching the region of interest (ROI). The electron beam scans a large area around the ROI (cf. Fig. 13). The showering intends to pin the contaminants, which form a layer of immobile contamination with small thickness. The showered region can then be investigated at higher magnification in a small ROI with reduced contamination growth because fewer mobile contaminants are available to diffuse into the ROI. However, this is not expected to be a permanent effect because contaminants will diffuse across the showered region (Mitchell, 2015).

To test the effectiveness of beam showering, an area of $21 \times 21\ \mu m^2$ on the aC film was scanned at 20 keV for 10 min using different measured beam currents of 32, 2,050, and 7,280 pA. The area varied slightly because it was chosen as the size of a grid window in the Cu grids supporting the aC film. Subsequently, a smaller $1 \times 1\ \mu m^2$ patch was scanned with 20 keV electrons and a beam current of 40 pA for 36 min. Scanning of the ROI was regularly interrupted to take HAADF-STEM images of the ROI and its vicinity to determine the average contamination thickness of the patch. The resulting average contamination thickness (Fig. 14a) increases with a varying rate depending on the current used for beam showering. The measurement without beam showering (blue symbols in Fig. 14a) shows the highest contamination rate with a thickness increase that is in good agreement with the long-time saturation test (Fig. 9). Beam showering with the smallest current of 33 pA (yellow symbols in Fig. 14a) already reduces contamination growth, especially in the first 10 min. Beam showering with higher currents (2,050 and 7,280 pA) suppresses contamination at small T even more. However, the reduction of $\overline{t_c}$ after 36 min of irradiation is not proportional to the current used for beam showering. High electron doses may damage the sample. Thus, it is a better idea to use moderate currents for beam showering. We note that the slope of all curves in Figure 14a become similar after longer illumination times. The contamination then continues to grow at a rate similar to the rate without beam showering. The cleaning effect of beam showering is, therefore, only temporary. However, beam showering with high currents can almost completely suppress contamination growth in the first few minutes.

The clearly defined area of beam showering and the observation that the contamination rate continues to grow at almost the same rate after a specific illumination time, independent of
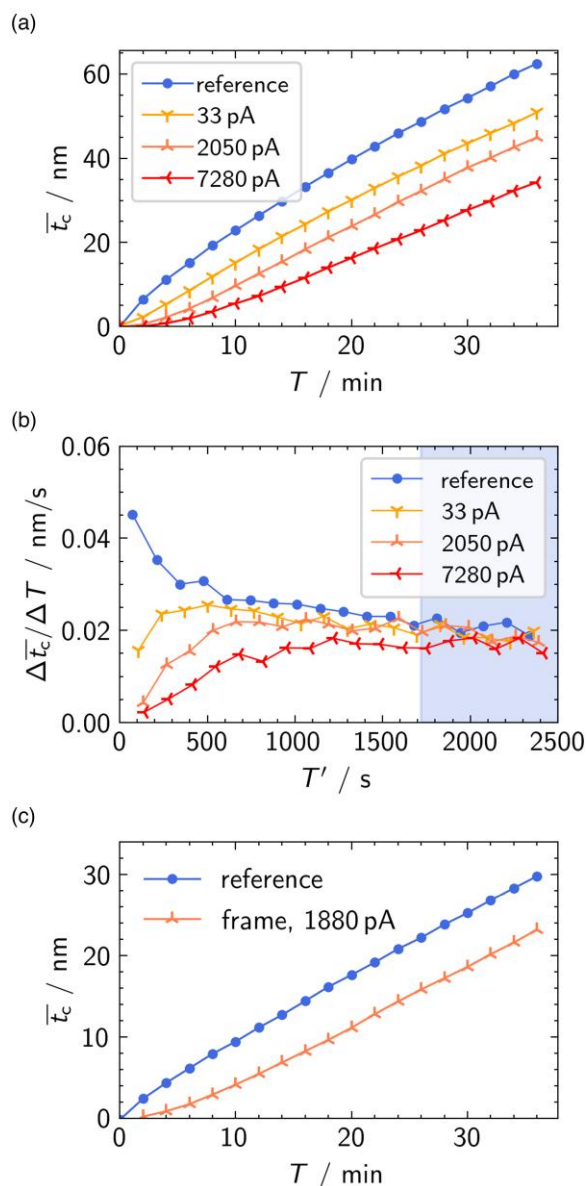
Fig. 14. (**a**) Average contamination thickness ($\overline{t_c}$) as a function of the irradiation time T after beam showering with (measured) currents given in the legend and without beam showering (reference). (**b**) Slope of the contamination growth curves in Figure 14a as a function of time T' after the beam showering with different beam currents. (**c**) Beam showering for electron-beam sensitive materials. A region of $3 \times 3\ \mu m^2$ in the center of the showered area was excluded. The average contamination thickness ($\overline{t_c}$) as a function of the irradiation time T is plotted without beam showering (reference) and after showering the area around the ROI only. Measurements performed at the Strata microscope.

the used beam showering current (Fig. 14a), allow conclusions on the mobility of contaminants on the surface. Directly after beam showering, mobile contaminants in the showered area are reduced because they are converted to immobile contamination. Due to the lack of mobile contaminants in the showered region, a gradient of contaminants exists between the showered region and the region further outside. This gradient leads to the diffusion of contaminants from further outside into the showered region. Contamination in the ROI continues to grow at the same rate as without beam showering if the diffusing molecules reach the ROI. This characteristic time T_D

depends on the diffusion constant, which can be derived from the data presented in Figure 14a.

The mean square displacement $x = \sqrt{k \cdot 2DT_D}$ is the average diffusion distance of a molecule. It depends on the dimensionality k of the system, the diffusion time T_D, and the diffusion coefficient D (Chatwin et al., 1998). In our beam-showering experiments, the shortest distance x is 10 μm from the border of the showered area to the ROI. The diffusion time T_D can be estimated by plotting the slope of the contamination curves in Figure 14a as a function of illumination time after beam showering (Fig. 14b). Figure 14b shows that similar slopes are obtained after an illumination time of about 1,700 s (28.5 min). Within this time, contaminants from outside the showered region reach the ROI, leading to enhanced contamination growth comparable to the reference measurement without showering. The evaluated diffusion constant for diffusing contaminant molecules on aC films in our experiments is

$$D = \frac{x^2}{2kT_D} = 1.5 \cdot 10^{-14} \frac{m^2}{s}, \qquad (8)$$

with the dimensionality of the system $k = 2$. This value is only a rough estimate, but still an interesting result because experimental data on surface diffusion coefficients of hydrocarbons is rarely found in literature. Our estimate of the diffusion constant is considerably smaller than other findings on diffusion constants of cyclic hydrocarbons (C_6H_6 and C_6H_{12}) on nickel (around 10^{-9} m^2/s) (Silverwood & Armstrong, 2018), but not too different from the estimate $D = 1.5 \cdot 10^{-15}$ m^2/s for contaminants on aC and $Pd_{77.5}Cu_6Si_{16.5}$ thin films (Hettler et al., 2017), and $D = 7.5 \cdot 10^{-14}$ m^2/s for contaminants on bulk Si (Rykaczewski et al., 2008). However, considerable variations of surface diffusion constants are not surprising because surface diffusion depends on the specific molecule/substrate system.

A modification of the beam-showering procedure for electron-beam sensitive materials is suggested considering the dominating role of surface diffusion. The setup in Figure 13 was slightly changed by leaving out a square of 3×3 μm^2 in the center of the showered area. The surrounding 25×25 μm^2 region was scanned for 10 min at 20 keV with a measured beam current of 1,880 pA. A 1×1 μm^2 contamination patch was then grown in the (non-illuminated) center ROI. As expected, contamination growth (red symbols in Fig. 14c) is also reduced because the contaminants in the non-irradiated ROI are quickly depleted, and only a small density of mobile contaminants is present in the showered surrounding region. We observe a similar contamination reduction as for the fully showered area (see the measurement labeled "2,050 pA" in Fig. 14a). A comparable approach with alternating showering and measurement might be even more effective (Bruenger, 1997).

Desorption of Contaminants by Sample Baking

Desorption of contaminant molecules from the sample surface is another frequently applied strategy to reduce contamination in electron microscopy (Hettler et al., 2017; Goh et al., 2020). This reduction is possible by increasing the sample temperature either in-situ in the microscope or before electron microscopy investigations if a heating sample holder is not available. In the following, we show results on the influence of external sample heating in a high-vacuum recipient. For this purpose, a
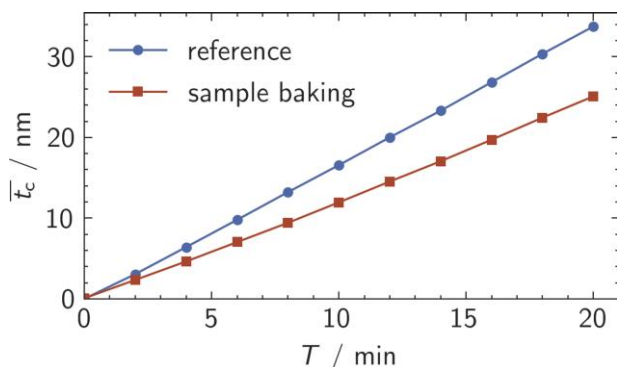

Fig. 15. Average contamination thickness ($\overline{t_c}$) as a function of irradiation time T for a baked aC-film sample (100°C for 15 min at a pressure of $4 \cdot 10^{-3}$ mbar) and a sample without cleaning as reference (Helios).

vacuum heating setup (TS 716, Binder Labortechnik, Hebertshausen, Germany) was used where the specimen in the sample holder of the Helios microscope was baked at 100°C for 15 min at a pressure of $4 \cdot 10^{-3}$ mbar. After baking, the total transfer time of the sample into the microscope was 3 min (2 min for venting and 1 min for insertion of the sample holder into the microscope). During this time, molecules from the surrounding air can adsorb again, which is expected to limit the efficiency of the technique.

Figure 15 compares the average contamination thickness as a function of illumination time for a baked and unbaked sample. Despite the moderate baking temperature and short baking time, $\overline{t_c}$ is distinctly reduced compared to the unbaked sample. The technique is thus recommendable for samples and sample holders that can withstand elevated temperatures. The heating of a sample in-situ in the microscope is expected to be even more efficient due to better vacuum conditions and the prevention of molecule adsorption during sample transfer into the microscope.

Plasma Cleaning

Plasma cleaning is a well-established and efficient technique for sample cleaning. External plasma cleaners and plasma cleaners installed at microscope chambers are available (Roberts et al., 1997; Isabell et al., 1999; Vladár et al., 2001; Mitchell, 2015). We tested the cleaning efficiency of 15 min in-chamber plasma cleaning, using the plasma cleaner (FEI plasma cleaner, 19 W, operated at ~50 Pa chamber pressure) installed at the chamber of the Helios microscope. The system was vented with N_2 for some seconds and pumped
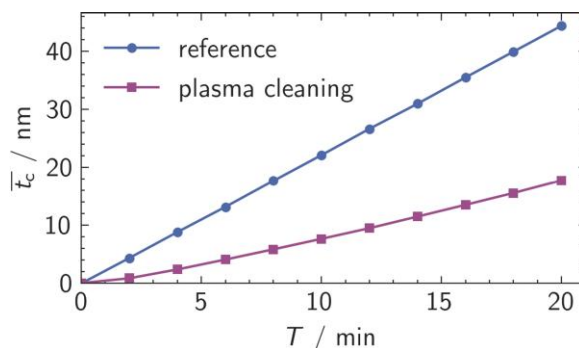

Fig. 16. Average contamination thickness ($\overline{t_c}$) as a function of irradiation time T for an aC film before (reference) and after plasma cleaning using (15 min at a chamber pressure of 50 Pa, Helios).
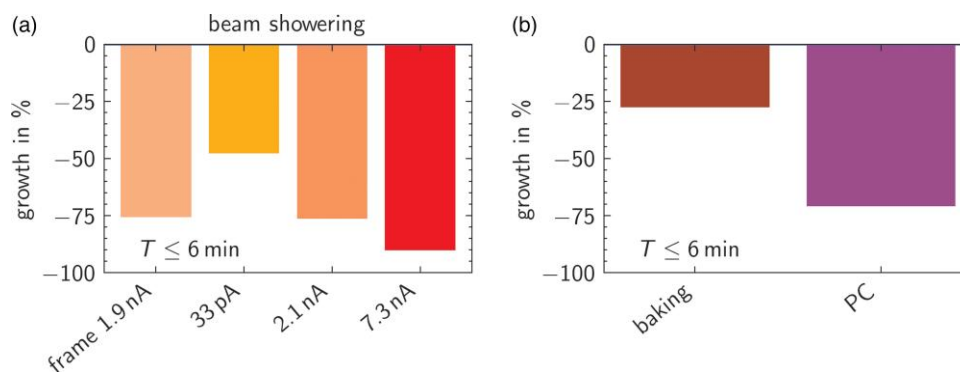
Fig. 17. Comparison of contamination-mitigation strategies. The reduction of contamination in percent is given by the ratio of the contamination growth rates after cleaning and the corresponding reference measurement without cleaning, evaluated for up to 6 min illumination time. (**a**) Beam showering tested in the Strata microscope with "frame" indicating that showering was not applied to the ROI, and (**b**) sample baking and plasma cleaning, tested in the Helios microscope.

down to 50 Pa (the reactive gas hence being N_2) before in-situ plasma cleaning. This means that not only the specimen is cleaned but also the sample holder and the microscope chamber.

Figure 16 shows the contamination growth before plasma cleaning (blue symbols) and on the same sample directly after plasma cleaning (purple symbols). Plasma cleaning proves to be very efficient because the contamination rate is substantially reduced even after 20 min of illumination. This behavior differs from beam showering, where the contamination rate increases after a few minutes to the rate of untreated samples. It indicates that contaminants are removed from the sample surface from a large area, leading to a long-lasting depletion of contaminant molecules. However, the plasma is potentially damaging for organic materials, and an oxygen-containing plasma leads to oxidation of numerous materials. This damage can be reduced by adjusting gas type and pressure, and plasma power. Hence, several parameters of plasma cleaning, like the gas type, the power, and the processing time of plasma cleaning (Zaluzec et al., 1997; Roberts et al., 2001), on different sample materials would be interesting to study and they could be well examined with our contamination-test procedure. Plasma cleaning the microscope and the specimen separately could also help to identify the source of contaminants. However, we limited the assessment of cleaning techniques to avoid overloading the paper.

Comparison of Contamination-Mitigation Strategies

In the following, we compare the efficiency of the different tested contamination-mitigation strategies. For this purpose, the reduction of contamination growth is shown in percent for each technique for illumination times up to 6 min (Fig. 17). The same evaluation for up to 20 min is presented in the Supporting Information (Supplementary Fig. 7), which illustrates the long-term efficiency of the tested techniques. The following scheme was used to calculate the reduction of contamination growth. We assume that the average contamination thickness increases linearly. The fitted slope of each measurement is then compared to the slope of the corresponding reference measurement, leading to directly comparable results.

Beam showering has not shown the same efficiency in the Strata and Helios microscopes, even when the same samples were used. It has shown only a tiny and short-lasting (<4 min) effect in the Helios microscope. In contrast, almost 100% reduction of contamination growth was achieved

within the first 6 min in the Strata microscope (Fig. 17a). An effect of beam showering in the Helios microscope was only found if a larger area was showered. This finding indicates that faster diffusing contaminants are present on the sample, possibly from the sample holder or the residual gas atmosphere in the microscope chamber.

The assumption of linear contamination growth is only a rough estimate, even for short illumination times. This applies in particular to beam showering because the contamination rate changes after a few minutes (Fig. 14a). As the cleaning effect of beam showering is only temporary, the determination of the growth rate over the 20 min underestimates the cleaning effect. Beam showering can be a good choice for short illumination times because it is easy to apply and does not require additional instrumentation. Beam showering without showering the ROI was only tested with one current. A similar contamination reduction compared to standard beam showering with a comparable current (2.1 nA) indicates that it is an even better choice for electron-beam sensitive samples. As previously discussed, beam showering is more effective for higher showering currents, but the efficiency is not improved proportionally to the showering current. A compromise is necessary considering the possible damage of the sample for high showering currents.

Sample baking and plasma cleaning were tested in the Helios microscope (Fig. 17b). Sample baking reduces contamination, but less than the other techniques. Sample baking and plasma cleaning treat the whole sample, leading to a longer-lasting effect than beam showering. In our case of in-situ plasma cleaning, even the microscope chamber is cleaned, as mentioned above. When illumination times up to 20 min are evaluated, the estimated effectivity of baking is similar to beam showering with the lowest current (cf. Supplementary Fig. 7). Plasma cleaning reduces contamination by about 70% in the first 6 min and maintains 60% efficiency after 20 min of irradiation.

Our findings agree well with the results obtained by Mitchell (2015), who stated that sample baking is effective but has to be applied for a longer time, best overnight, whereas plasma cleaning is faster than baking. He also found beam showering to be the fastest technique but only effective for a limited time.

Conclusions

Carbon contamination on electron-transparent aC films was investigated at electron energies of 30 keV and below in

SEMs in this work. A method was developed to measure the contamination thickness by quantitative evaluation of HAADF-STEM-in-SEM images. Reference measurements, always using the same parameters (electron energy, beam current) and the same specimen, are essential before contamination tests to monitor changes in the experimental system (microscope and specimen). Reference measurements could be useful in the future to test the success of empirical measures to reduce contamination, e.g., by extended plasma cleaning of the microscope chamber.

Most experiments in this work were performed with scanning (S(T)EM-like) illumination. The influence of essential imaging parameters (electron energy, beam current (dose rate), total electron dose) on the contamination thickness on thin aC films was investigated with the following conclusions regarding the minimization of contamination growth.

- The contamination increases with the total electron dose.
- For the same total dose, a high beam current (high dose rate) and short illumination time are favorable.
- The electron energy should be maximized if knock-on damage is not an issue.

Further quantitative studies of contamination on other materials (material classes) will be interesting to see if the same general behavior is observed.

The following strategies for contamination mitigation were tested regarding their efficiency:

- Beam showering can efficiently prevent contamination for a short irradiation-time interval in the order of a few minutes. The effectivity of beam showering increases with the showering current but saturates at high beam currents.
- Beam showering is still effective if it is only applied *around* the ROI, which protects the ROI from irradiation before the actual imaging.
- In-chamber plasma cleaning is an effective and long-lasting option for reducing contamination if the sample can withstand it.
- Short-time (15 min) sample baking at $100^{\circ}C$ in an external vacuum recipient is less effective than plasma cleaning. It can be applied if a sample cannot withstand plasma cleaning but sustains elevated temperatures.

However, we note that the efficiency of contamination strategies can vary depending on the system status (microscope and sample).

Beam showering experiments could be exploited to estimate the diffusion coefficient of contaminant molecules ($D \sim 10^{-14}$ m^2/s). This strategy is promising to test surface diffusion on other sample materials in the future.

The model developed by Müller was used to calculate the contamination thickness (Müller, 1969). An analytical solution is only available for TEM-like (homogeneous stationary) illumination, which describes the experimental results in this work well. Comparing theory and experimental data yields estimates of parameters that are otherwise not accessible (e.g., contamination cross-section, partial pressure of hydrocarbons, residence time of adsorbed hydrocarbons).

The comparability of the results with the measurement method presented in this work facilitates further investigations of sample cleaning parameters (applied time, applied dose/temperature/power) and different samples in the future. In any case, it should be kept in mind that reducing the contamination (rate) is not the only quality measure for a cleaning strategy, but also user-friendliness and possible sample damage.

Availability of data and materials

The raw data of this study (Hugenschmidt et al., 2022*a*) and a Python library demonstrating the thickness determination (Hugenschmidt et al., 2022*b*) are available.

Supplementary material

To view supplementary material for this article, please visit https://doi.org/10.1093/micmic/ozac003.

Author contributions statement

M.H. prepared the samples, carried out the TEM and part of the STEM measurements, and analyzed the data. The manuscript was written by M.H. and D.G. K.A and A.M. performed S(T)EM measurements and contributed to the data analysis. K.A. prepared the exemplary Python library for the supporting material from the data evaluation scripts written by M.H. and K.A. E.M. contributed substantially to the design of experiments and the discussion of results. D.G. initiated and supervised the project. All authors read the manuscript and contributed to the discussions of results.

Conflict of interest

The authors declare that they have no competing interest.

References

Alman DA, Ruzic DN & Brooks JN (2000). A hydrocarbon reaction model for low temperature hydrogen plasmas and an application to the Joint European Torus. *Phys Plasmas* **7**, 1421–1432.

Amman M (1996). Atomic force microscopy study of electron beam written contamination structures. *J Vac Sci Technol B Microelectron Nanometer Struct—Process Meas Phenom* **14**, 54.

Bance UR, Drummond IW, Finbow D, Harden EH & Kenway P (1978). 27. Hydrocarbon contamination in vacuum dependent scientific instruments. *Vacuum* **28**, 489–496.

Bruenger WH (1997). Contamination reduction in low voltage electron-beam microscopy for dimensional metrology. *J Vac Sci Technol B Microelectron Nanometer Struct—Process Meas Phenom* **15**, 2181.

Chatwin P, Dagan G, List J, Mei C, Savage S & Grathwohl P (1998). *Diffusion in Natural Porous Media: Contaminant Transport, Sorption/Desorption and Dissolution Kinetics*. Boston, MA: Springer US.

Christy RW (1960). Formation of thin polymer films by electron bombardment. *J Appl Phys* **31**, 1680–1683.

Conru HW & Laberge PC (1975). Oil contamination with the SEM operated in the spot scanning mode. *J Phys E Sci Instrum* **8**, 136–138.

Demers H, Poirier-Demers N, Couture AR, Joly D, Guilmain M, de Jonge N & Drouin D (2011). Three-dimensional electron microscopy simulation with the CASINO Monte Carlo software. *Scanning* **33**, 135–146.

Dyck O, Kim S, Kalinin SV & Jesse S (2018). Mitigating e-beam-induced hydrocarbon deposition on graphene for atomic-scale scanning transmission electron microscopy studies. *J Vac Sci Technol B Nanotechnol Microelectron Mater Process Meas Phenom* **36**, 11801.

Egerton RF (2019). Radiation damage to organic and inorganic specimens in the TEM. *Micron* **119**, 72–87.

Egerton RF & Rossouw CJ (1976). Direct measurement of contamination and etching rates in an electron beam. *J Phys D Appl Phys* **9**, 659–663.

Ennos AE (1953). The origin of specimen contamination in the electron microscope. *Br J Appl Phys* **4**, 101–106.

Ennos AE (1954). The sources of electron-induced contamination in kinetic vacuum systems. *Br J Appl Phys* **5**, 27–31.

Fowlkes JD, Randolph SJ & Rack PD (2005). Growth and simulation of high-aspect ratio nanopillars by primary and secondary electron-induced deposition. *J Vac Sci Technol B Microelectron Nanometer Struct—Process Meas Phenom* **23**, 2825.

Goh YM, Schwartz J, Ma T, Kerns B & Hovden R (2020). Open-hardware, high-vacuum storage for TEM holders remedies and quantifies hydrocarbon contamination. *Microsc Microanal* **26**, 3120–3123.

Griffiths AJV & Walther T (2010). Quantification of carbon contamination under electron beam irradiation in a scanning transmission electron microscope and its suppression by plasma cleaning. *J Phys Conf Ser* **241**, 12017.

Heide HG (1963). Die Objektverschmutzung im Elektronenmikroskop und das Problem der Strahlenschädigung durch Kohlenstoffabbau. *Z Angew Phys* **15**, 116–128.

Hettler S, Dries M, Hermann P, Obermair M, Gerthsen D & Malac M (2017). Carbon contamination in scanning transmission electron microscopy and its impact on phase-plate applications. *Micron* **96**, 38–47.

Hillier J (1948). On the investigation of specimen contamination in the electron microscope. *J Appl Phys* **19**, 226–230.

Hirsch EH (1960). Image formation by electron bombardment of metal targets. *Br J Appl Phys* **11**, 547–550.

Hirsch EH (1977). The growth of carbonaceous contamination on surfaces undergoing ion bombardment. *J Phys D Appl Phys* **10**, 2069–2076.

Hirsch P, Kässens M, Püttmann M & Reimer L (1994). Contamination in a scanning electron microscope and the influence of specimen cooling. *Scanning* **16**, 101–110.

Horiuchi S, Hanada T, Ebisawa M, Matsuda Y, Kobayashi M & Takahara A (2009). Contamination-free transmission electron microscopy for high-resolution carbon elemental mapping of polymers. *ACS Nano* **3**, 1297–1304.

Hoyle D, Malac M, Trudeau M & Woo P (2011). UV treatment of TEM/STEM samples for reduced hydrocarbon contamination. *Microsc Microanal* **17**, 1026–1027.

Hren JJ (1978). Specimen contamination in analytical electron microscopy: Sources and solutions. *Ultramicroscopy* **3**, 375–380.

Hugenschmidt M, Adrion K, Marx A, Müller E & Gerthsen D (2022a). Raw data for "Electron-beam-induced carbon contamination in STEM-in-SEM: Quantification and mitigation". https://doi.org/10.5281/zenodo.6425001

Hugenschmidt M, Adrion K, Marx A, Müller E & Gerthsen D (2022b). Supplementary data and information for "Electron-beam-induced carbon contamination in STEM-in-SEM: Quantification and mitigation". https://doi.org/10.5281/zenodo.6425118

Hugenschmidt M, Müller E & Gerthsen D (2019). Electron beam broadening in electron-transparent samples at low electron energies. *J Microsc* **274**, 150–157.

Isabell TC, Fischione PE, O'Keefe C, Guruz MU & Dravid VP (1999). Plasma cleaning and its applications for electron microscopy. *Microsc Microanal* **5**, 126–135.

Kanaya K, Oho E, Osaki N & Oda T (1988). A contamination reducing method by ion beam bombardment of the specimen in high resolution electron microscopy. *Micron Microsc Acta* **19**, 163–173.

Kanaya K, Yonehara K, Oho E, Inoue N & Izumida M (1990). A cone formation theory of contamination in high resolution transmission electron microscopy. *Micron Microsc Acta* **21**, 13–28.

Knox WA (1976). Contamination formed around a very narrow electron beam. *Ultramicroscopy* **1**, 175–180.

Kumao A, Hashimoto H & Shiraishi (1981). Studies on specimen contamination by transmission electron microscopy. *J Electron Microsc* **30**, 161–170.

Lau D, Hughes AE, Muster TH, Davis TJ & Glenn AM (2010). Electron-beam-induced carbon contamination on silicon: Characterization using Raman spectroscopy and atomic force microscopy. *Microsc Microanal* **16**, 13–20.

Li W & Joy DC (2006). Study of temperature influence on electron beam induced deposition. *J Vac Sci Technol, A* **24**, 431–436.

Li C, Tardajos AP, Da Wang, Choukroun D, van Daele K, Breugelmans T & Bals S (2021). A simple method to clean ligand contamination on TEM grids. *Ultramicroscopy* **221**, 113195.

Lin Y & Joy DC (2005). A new examination of secondary electron yield data. *Surf Interface Anal* **37**, 895–900.

Lobo CJ, Toth M, Wagner R, Thiel BL & Lysaght M (2008). High resolution radially symmetric nanostructures from simultaneous electron beam induced etching and deposition. *Nanotechnology* **19**, 25303.

Love G, Scott vd, Dennis NMT & Laurenson L (1981). Sources of contamination in electron optical equipment. *Scanning* **4**, 32–39.

Materna Mikmeková E, Müllerová I, Frank L, Paták A, Polčák J, Sluyterman S, Lejeune M & Konvalina I (2020). Low-energy electron microscopy of graphene outside UHV: Electron-induced removal of PMMA residues used for graphene transfer. *J Electron Spectrosc Relat Phenom* **241**, 146873.

McGilvery CM, Goode AE, Shaffer MSP & McComb DW (2012). Contamination of holey/lacey carbon films in STEM. *Micron* **43**, 450–455.

Mikmeková E, Frank L, Müllerová I, Li BW, Ruoff RS & Lejeune M (2016). Study of multi-layered graphene by ultra-low energy SEM/STEM. *Diamond Relat Mater* **63**, 136–142.

Mitchell DRG (2015). Contamination mitigation strategies for scanning transmission electron microscopy. *Micron* **73**, 36–46.

Mitsuishi K, Liu ZQ, Shimojo M, Han M & Furuya K (2005). Dynamic profile calculation of deposition resolution by high-energy electrons in electron-beam-induced deposition. *Ultramicroscopy* **103**, 17–22.

Müller K-H (1969). *Elektronen-Mikroschreiber mit geschwindigkeitsgesteuerter Strahlführung*. Tübingen: Eberhard-Karls-Universität zu Tübingen.

Pinard PT (2016). *Electron Probe Microanalysis of Carbon Containing Steels at a High Spatial Resolution*. Aachen: RWTH Aachen University.

Postek MT (1996). An approach to the reduction of hydrocarbon contamination in the scanning electron microscope. *Scanning* **18**, 269–274.

Reimer L (1998). *Scanning Electron Microscopy: Physics of Image Formation and Microanalysis*. Berlin: Springer.

Reimer L & Wächter M (1978). Contribution to the contamination problem in transmission electron microscopy. *Ultramicroscopy* **3**, 169–174.

Roberts S, McCaffrey J, Giannuzzi L, Stevie F & Zaluzec NJ (2001). Advanced techniques in TEM specimen preparation. In *Progress in Transmission Electron Microscopy 1: Concepts and Techniques*, Zhang X-F & Zhang Z (Eds.), pp. 343–351. Berlin: Springer.

Roberts SP, Zaluzec NJ, Walck SD & Grant JT (1997). Applications of reactive gas plasma cleaning technology in minimizing contamination of specimens during transmission and analytical electron microscopy. *MRS Proc* **480**, 127–136.

Roediger P, Wanzenboeck HD, Hochleitner G & Bertagnolli E (2009). Evaluation of chamber contamination in a scanning electron microscope. *J Vac Sci Technol B Microelectron Nanometer Struct—Process Meas Phenom* **27**, 2711.

Rykaczewski K, Marshall A, White WB & Fedorov AG (2008). Dynamic growth of carbon nanopillars and microrings in electron beam induced dissociation of residual hydrocarbons. *Ultramicroscopy* **108**, 989–992.

Rykaczewski K, White WB & Fedorov AG (2007). Analysis of electron beam induced deposition (EBID) of residual hydrocarbons in electron microscopy. *J Appl Phys* **101**, 54307.

Sasaki T, Sawada H, Hosokawa F, Sato Y & Suenaga K (2014). Aberration-corrected STEM/TEM imaging at 15kV. *Ultramicroscopy* **145**, 50–55.

Sawada H, Sasaki T, Hosokawa F & Suenaga K (2015). Atomic-Resolution STEM Imaging of Graphene at Low Voltage of 30 kV with Resolution Enhancement by Using Large Convergence Angle. *Phys Rev Lett* **114**, 166102.

Schiffmann KI (1993). Investigation of fabrication parameters for the electron-beam-induced deposition of contamination tips used in atomic force microscopy. *Nanotechnology* **4**, 163–169.

Schweizer P, Dolle C, Dasler D, Abellán G, Hauke F, Hirsch A & Spiecker E (2020). Mechanical cleaning of graphene using in situ electron microscopy. *Nat Commun* **11**, 1743.

Silverwood IP & Armstrong J (2018). Surface diffusion of cyclic hydrocarbons on nickel. *Surf Sci* **674**, 13–17.

Smith DA (2007). *Elucidating the Growth Mechanisms of Electron Beam Induced Deposition via a Three Dimensional, Monte-Carlo Based Simulation*. Knoxville: University of Tennessee.

Soong C, Woo P & Hoyle D (2012). Contamination cleaning of TEM/SEM samples with the ZONE cleaner. *Microsc Today* **20**, 44–48.

Stewart RL (1934). Insulating films formed under electron and Ion bombardment. *Phys Rev* **45**, 488–490.

Tomita T, Harada Y, Watanabe H & Etoh T (1979). Reduction of contamination in analytical electron microscopy. *Shinku (1958-2007)* **22**, 158–164.

Ueda K & Yoshimura M (2004). Fabrication of nanofigures by focused electron beam-induced deposition. *Thin Solid Films* **464-465**, 331–334.

Utke I, Hoffmann P & Melngailis J (2008). Gas-assisted focused electron beam and ion beam processing and fabrication. *J Vac Sci Technol B Microelectron Nanometer Struct—Process Meas Phenom* **26**, 1197.

van Dorp WF & Hagen CW (2008). A critical literature review of focused electron beam induced deposition. *J Appl Phys* **104**, 81301.

Vladár AE & Postek M (2005). Electron beam-induced sample contamination in the SEM. *Microsc Microanal* **11**, 764–765.

Vladár AE, Postek JT & Vane R (2001). Active monitoring and control of electron-beam-induced contamination. In *Metrology, Inspection, and Process Control for Microlithography XV*, Sullivan NT (Ed.), pp. 835. Santa Clara, CA: SPIE.

Vladár AE, Purushotham KP & Postek MT (2008). Contamination specification for dimensional metrology SEMs. In *Metrology, Inspection, and Process Control for Microlithography XXII*, Allgair JA & Raymond CJ (Eds.), pp. 692217. San Jose, CA: SPIE.

Wall JS (1980). Contamination in the STEM at ultra high vacuum. *Scan Electron Microsc*, 99–106.

Wanzenboeck HD, Roediger P, Hochleitner G, Bertagnolli E & Buehler W (2010). Novel method for cleaning a vacuum chamber from hydrocarbon contamination. *J Vac Sci Technol A* **28**, 1413–1420.

Watson JHL (1947). An effect of electron bombardment upon carbon black. *J Appl Phys* **18**, 153–161.

Zaluzec NJ, Kestel BJ & Henriks D (1997). Reactive gas plasma specimen processing for use in microanalysis and imaging in analytical electron microscopy. *Microsc Microanal* **3**, 983–984.